

## Upscale versus “Up-Amplitude” Growth of Forecast-Error Spectra

RICHARD ROTUNNO<sup>1</sup>,<sup>a</sup> CHRIS SNYDER,<sup>a</sup> AND FALKO JUDT<sup>a</sup>

<sup>a</sup> National Center for Atmospheric Research, Boulder, Colorado

(Manuscript received 23 March 2022, in final form 7 September 2022)

**ABSTRACT:** Atmospheric predictability is measured by the average difference (or “error”) within an ensemble of forecasts starting from slightly different initial conditions. The spatial scale of the error field is a fundamental quantity; for meteorological applications, the error field typically varies with latitude and longitude and so requires a two-dimensional (2D) spectral analysis. Statistical predictability theory is based on the theory of homogeneous, isotropic turbulence, in which spectra are circularly symmetric in 2D wavenumber space. One takes advantage of this circular symmetry to reduce 2D spectra to one-dimensional (1D) spectra by integrating around a circle in wavenumber polar coordinates. In recent studies it has become common to reduce 2D error spectra to 1D by computing spectra in the zonal direction and then averaging the results over latitude. It is shown here that such 1D error spectra are generically fairly constant across the low wavenumbers as the amplitude of an error spectrum grows with time and therefore the error spectrum is said grow “up-amplitude.” In contrast computing 1D error spectra in a manner consistent with statistical predictability theory gives spectra that are peaked at intermediate wavenumbers. In certain cases, this peak wavenumber is decreasing with time as the error at that wavenumber increases and therefore the error spectrum is said to grow “upscale.” We show through theory, simple examples, and global predictability experiments that comparisons of model error spectra with the predictions of statistical predictability theory are only justified when using a theory-consistent method to transform a 2D error field to a 1D spectrum.

**KEYWORDS:** Error analysis; Fourier analysis; Numerical weather prediction/forecasting; Diagnostics

### 1. Introduction

A basic metric for estimating atmospheric predictability is the average difference (or “error”) within an ensemble of forecasts starting from slightly different initial conditions. It is often useful to estimate the spatial scale of the error field and spectral analysis is the natural tool to do so. For meteorological applications, the error field of interest will vary with latitude and longitude ( $x, y$ ), which requires a two-dimensional (2D) spectral analysis in wavenumbers ( $k, l$ ). Statistical predictability theory (Lesieur 2008, chapter 11) is based on the theory of homogeneous, isotropic turbulence, in which spectra are circularly symmetric in  $k$ – $l$  space. Statistical predictability theory takes advantage of this circular symmetry to reduce two-dimensional spectra in  $k$ – $l$  space to one-dimensional (1D) spectra in the polar coordinates  $(\kappa, \theta) = (\sqrt{k^2 + l^2}, \tan^{-1}l/k)$  in which the spectra are independent of  $\theta$ . In recent studies it has become common in meteorological analyses to reduce 2D error spectra to 1D error spectra by computing spectra in the  $x$  direction and then averaging the results over  $y$ . The objective of this paper is to show that the latter procedure produces 1D error spectra that, except for power-law spectra, fail to capture important aspects of statistical predictability theory.

Statistical predictability theory began with Lorenz (1969) in which the predictability problem was formulated in terms of the growth of small initial differences in a statistically stationary, homogeneous, isotropic turbulent flow; studies followed using more sophisticated turbulence models (Lesieur 2008, chapter 11). These studies find that the growth of the peak

scale and amplitude of an error energy spectrum depends on the energy spectrum of the assumed background turbulent flow. For a background turbulent flow with the power-law spectrum  $\kappa^{-\beta}$ , the time scale for the error-spectrum evolution, including the increase of the peak scale  $\kappa_{\text{peak}}^{-1}$  and amplitude, is inversely proportional to  $\kappa_{\text{peak}}$  for  $\beta = 5/3$  and constant when  $\beta = 3$  (Lesieur 2008, 412–413). For the “–5/3” case the inverse dependence of error-scale and amplitude growth rate on scale implies limited predictability since confining an initial error to ever smaller scales implies ever faster error growth rates. For the “–3” case, the peak scale of error energy is determined by the peak scale in the background energy spectrum; confining the initial error to ever smaller scales refines the initial condition without introducing faster error growth implying unlimited intrinsic predictability. Note that in both the 3D and 2D cases, the theoretical error spectra for  $\kappa < \kappa_{\text{peak}}$  have fixed slopes ( $\kappa^4$  in 3D and  $\kappa^3$  in 2D) and therefore grow along with the error amplitude at  $k_{\text{peak}}$  (Lesieur 2008, Figs. 11.2–11.3). Thus, the error spectra for  $\kappa < \kappa_{\text{peak}}$  could be described as growing “up-amplitude,” but the emphasis on this feature would be misplaced since it is the growth of the peak-error scale and amplitude that characterize the evolution of the theoretical error energy spectrum. The determination of the peak scale  $\kappa_{\text{peak}}^{-1}$  through spectral analysis in a manner consistent with statistical predictability theory is the issue addressed in the following.

To economize the writing, the reduction of a spectrum from 2D to 1D by integrating in  $\theta$  in polar coordinates in wavenumber space is termed a 1D $\kappa$  spectrum while the reduction of a spectrum from 2D to 1D by transforming in  $x$  (which gives the transform as a function of wavenumber  $k$  and  $y$ ) and then averaging over  $y$  is termed a 1D $k$  spectrum. The error

Corresponding author: Richard Rotunno, rotunno@ucar.edu

DOI: 10.1175/JAS-D-22-0070.1

© 2022 American Meteorological Society. For information regarding reuse of this content and general copyright information, consult the AMS Copyright Policy ([www.ametsoc.org/PUBSReuseLicenses](http://www.ametsoc.org/PUBSReuseLicenses)).

Brought to you by University of Colorado Libraries | Unauthenticated | Downloaded 06/09/23 10:00 PM UTC

spectra at a particular wavenumber is said to be “saturated” when it reaches the level of the background energy spectrum.

Figure 5 of [Mapes et al. \(2008\)](#) compares the theoretical  $1D\kappa$  error spectra of [Rotunno and Snyder \(2008\)](#) to the  $1Dk$  error spectra at the equator<sup>1</sup> from a high-resolution global meteorological model (their Fig. 5c). The  $1Dk$  error spectra are observed “... to fill up the saturation spectrum vertically (up-amplitude) rather than horizontally (upscale). Large scales grow just as rapidly as small scales, and they do so before small scales saturate.” In other words, the analyzed  $1Dk$  error spectra are essentially constant from  $k = 0$  to  $k_{\text{sat}}$ , where  $k_{\text{sat}}$  is the wavenumber at which the  $1Dk$  error spectra equal the background energy spectrum. As the error spectra grow with time  $t$ , they preserve the “flat-line” shape from  $k = 0$  to  $k_{\text{sat}}(t)$  which decreases with  $t$ , and so growth of the error spectra is said to be “up-amplitude.” In contrast, the theoretical  $1D\kappa$  error spectra increase with  $\kappa$  from  $\kappa = 0$  to a peak at  $\kappa_{\text{sat}}(t)$  in the case of a “ $-5/3$ ” background energy spectrum. Since the peak wavenumber decreases with  $t$ , the growth of the  $1D\kappa$  error spectra is said to be upscale. Further discussion of the case with a “ $-3$ ” background spectrum is given in [section 4](#).

[Durrán et al. \(2013\)](#) compute  $1Dk$  (including ensemble averaging) error spectra in a case study of predictability using a limited-area forecast model. Similar to the conclusion in [Mapes et al. \(2008\)](#), [Durrán et al. \(2013, Abstract\)](#) find, “There is no evidence of small-scale perturbations developing rapidly and transferring their influence upscale. Instead, the large-scale perturbations appear to grow more rapidly during the first 12 h than those at the smallest resolved scales.” The same conclusion is reached in [Weyn and Durrán \(2017, Abstract\)](#) in the context of a simulation of an idealized mesoscale convective system: “Both small- and large-scale errors grow primarily up in amplitude at all scales rather than through an upscale cascade between adjacent scales.” Most recently, [Lloveras et al. \(2021\)](#), in the context of numerical simulations of idealized baroclinic waves with moist convection, note w.r.t their

Fig. 16 the difference in the shapes of the low-wavenumber parts of the  $1Dk$  (constant with  $k$ ) and  $1D\kappa$  (increasing with  $\kappa$ ) error spectra but conclude: “Nevertheless, the error growth using both computational methods is primarily up-amplitude, with relative errors growing at approximately the same rate at all scales, rather than through an upscale cascade.”

In the present paper, we show that  $1D\kappa$  and  $1Dk$  error spectra are generally not the same and, moreover, they differ systematically over the low wavenumbers. Statistical predictability theory has  $1D\kappa$  error spectra increasing with  $\kappa$  up to  $\kappa_{\text{peak}}$  for both “ $-5/3$ ” and “ $-3$ ” background spectra ([Lesieur 2008](#), chapter 11), where the subscript “peak” signifies the wavenumber at which the error spectrum is a maximum. Here we show that an error field with a circularly symmetric 2D error spectrum has a  $1D\kappa$  spectrum that increases with  $\kappa$  up to  $\kappa_{\text{peak}}$  at the low wavenumbers, while the  $1Dk$  spectrum computed from the *same* error field is constant-with- $k$  up to  $k_{\text{peak}}$ .

In [section 2](#), the analytical/computational methods are developed for comparing  $1D\kappa$  and  $1Dk$  spectra. Simple examples based on arbitrary homogeneous, isotropic random functions are discussed in [section 3](#). The relevance of these examples to analyses of error spectra in a high-resolution global model ([Judt 2018, 2020](#)) is discussed in [section 4](#). Suggestions are made in [section 5](#) for how to compute local  $1D\kappa$  error spectra, which is of interest when the error fields are spatially inhomogeneous as in most realistic applications. Conclusions are summarized in [section 6](#).

## 2. Discrete Fourier analysis

The analysis here is similar to that of [Durrán et al. \(2017\)](#) but with emphasis on the relation between  $1D\kappa$  and  $1Dk$  error spectra.

The two-dimensional (2D) finite FT of the discrete function  $f(x_n, y_m) (= f_{n,m})$  is

$$F_{k,l} = \sum_{n=1}^{N_x} \sum_{m=1}^{N_y} f_{n,m} \exp\left\{-2\pi i \left[ \frac{(k-1)(n-1)}{N_x} + \frac{(l-1)(m-1)}{N_y} \right]\right\}; \quad 1 \leq k \leq N_x, \quad 1 \leq l \leq N_y, \quad (1)$$

with inverse

$$f_{n,m} = \frac{1}{N_x N_y} \sum_{k=1}^{N_x} \sum_{l=1}^{N_y} F_{k,l} \exp\left\{2\pi i \left[ \frac{(k-1)(n-1)}{N_x} + \frac{(l-1)(m-1)}{N_y} \right]\right\}; \quad 1 \leq n \leq N_x, \quad 1 \leq m \leq N_y. \quad (2)$$

The “energy”

$$E = \sum_{n=1}^{N_x} \sum_{m=1}^{N_y} (f_{n,m})^2 = \frac{1}{N_x N_y} \sum_{k=1}^{N_x} \sum_{l=1}^{N_y} |F_{k,l}|^2 \quad (3)$$

by Parseval’s theorem; the energy spectral density or “power spectrum” is  $|F_{k,l}|^2 (N_x N_y)^{-1}$ .

The one-dimensional (1D) finite FT of  $f(x_n, y_m)$  in  $x$  is

$$F_{k,m}^{1D} = \sum_{n=1}^{N_x} f_{n,m} \exp\left\{-2\pi i \left[ \frac{(k-1)(n-1)}{N_x} \right]\right\}; \quad 1 \leq k \leq N_x, \quad (4)$$

<sup>1</sup> The grid cell at the equator represents an average over latitude.

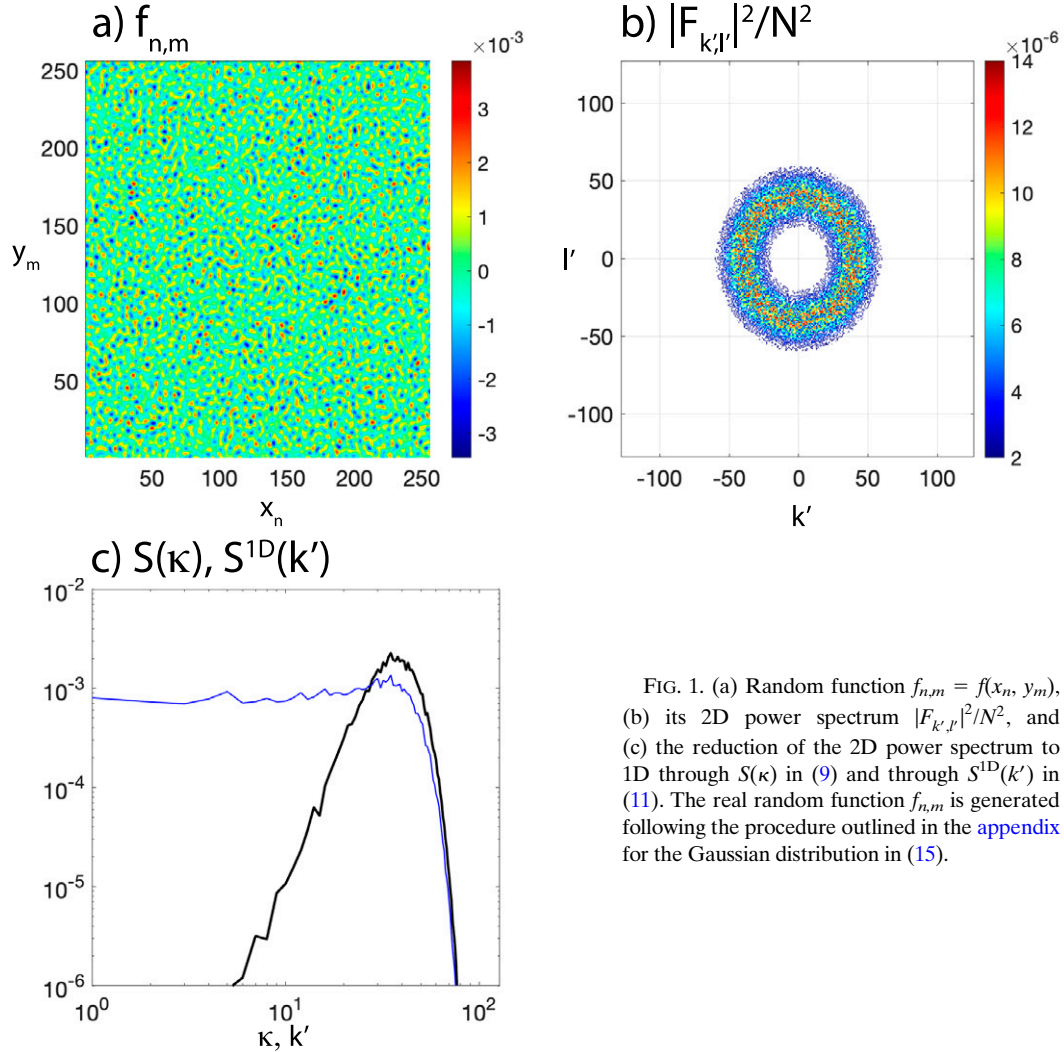


FIG. 1. (a) Random function  $f_{n,m} = f(x_n, y_m)$ , (b) its 2D power spectrum  $|F_{k,l}|^2/N^2$ , and (c) the reduction of the 2D power spectrum to 1D through  $S(\kappa)$  in (9) and through  $S^{1D}(k')$  in (11). The real random function  $f_{n,m}$  is generated following the procedure outlined in the [appendix](#) for the Gaussian distribution in (15).

with inverse

$$f_{n,m} = \frac{1}{N_x} \sum_{k=1}^{N_x} F_{k,m}^{1D} \exp\left\{2\pi i \left[ \frac{(k-1)(n-1)}{N_x} \right]\right\}; 1 \leq n \leq N_x. \quad (5)$$

The energy

$$E_m^{1D} = \sum_{n=1}^{N_x} (f_{n,m})^2 = \frac{1}{N_x} \sum_{k=1}^{N_x} |F_{k,m}^{1D}|^2 \quad (6)$$

by Parseval's theorem; the  $y_m$ -dependent power spectrum is  $|F_{k,m}^{1D}|^2 N_x^{-1}$ . The average of  $E_m^{1D}$  over  $y_m$  is

$$E^{1D} = \frac{1}{N_y} \sum_{n=1}^{N_x} \sum_{m=1}^{N_y} (f_{n,m})^2 = \frac{1}{N_x N_y} \sum_{k=1}^{N_x} \sum_{m=1}^{N_y} |F_{k,m}^{1D}|^2. \quad (7)$$

The 2D power spectrum,  $|F_{k,l}|^2 (N_x N_y)^{-1}$ , can be directly compared to the 1D power spectrum in the  $x$  direction,  $|F_{k,m}^{1D}|^2 N_x^{-1}$  as follows. Consider  $F_{k,m}^{1D}$  as a function of  $y_m$  and

note that its 1D finite Fourier transform in  $y_m$  is  $F_{k,l}$ . Using Parseval's theorem in the  $y_m$  direction then gives

$$\sum_{m=1}^{N_y} |F_{k,m}^{1D}|^2 = \frac{1}{N_y} \sum_{l=1}^{N_y} |F_{k,l}|^2,$$

which, upon division by  $N_x N_y$ , gives

$$\frac{1}{N_y} \sum_{m=1}^{N_y} |F_{k,m}^{1D}|^2 N_x^{-1} = \frac{1}{N_y} \sum_{l=1}^{N_y} |F_{k,l}|^2 (N_x N_y)^{-1}, \quad (8)$$

which says that the  $y_m$ -averaged-1D power spectrum is equal to the  $l$ -averaged 2D power spectrum.

The discrete 2D spectrum  $|F_{k,l}|^2$  is typically reduced to a 1D spectrum by summation within discrete annuli in wavenumber space ([Errico 1985](#)). For the purposes of the following demonstration, we take  $N_x = N_y = N$  and let  $(k', l') = (k-1, l-1)$  for  $k \leq N/2, l \leq N/2$ , and  $(k', l') = (-N-1+k, -N-1+l)$  for  $k \geq N/2+1, l \geq N/2+1$ , so that  $k' = l' = 0$  defines the

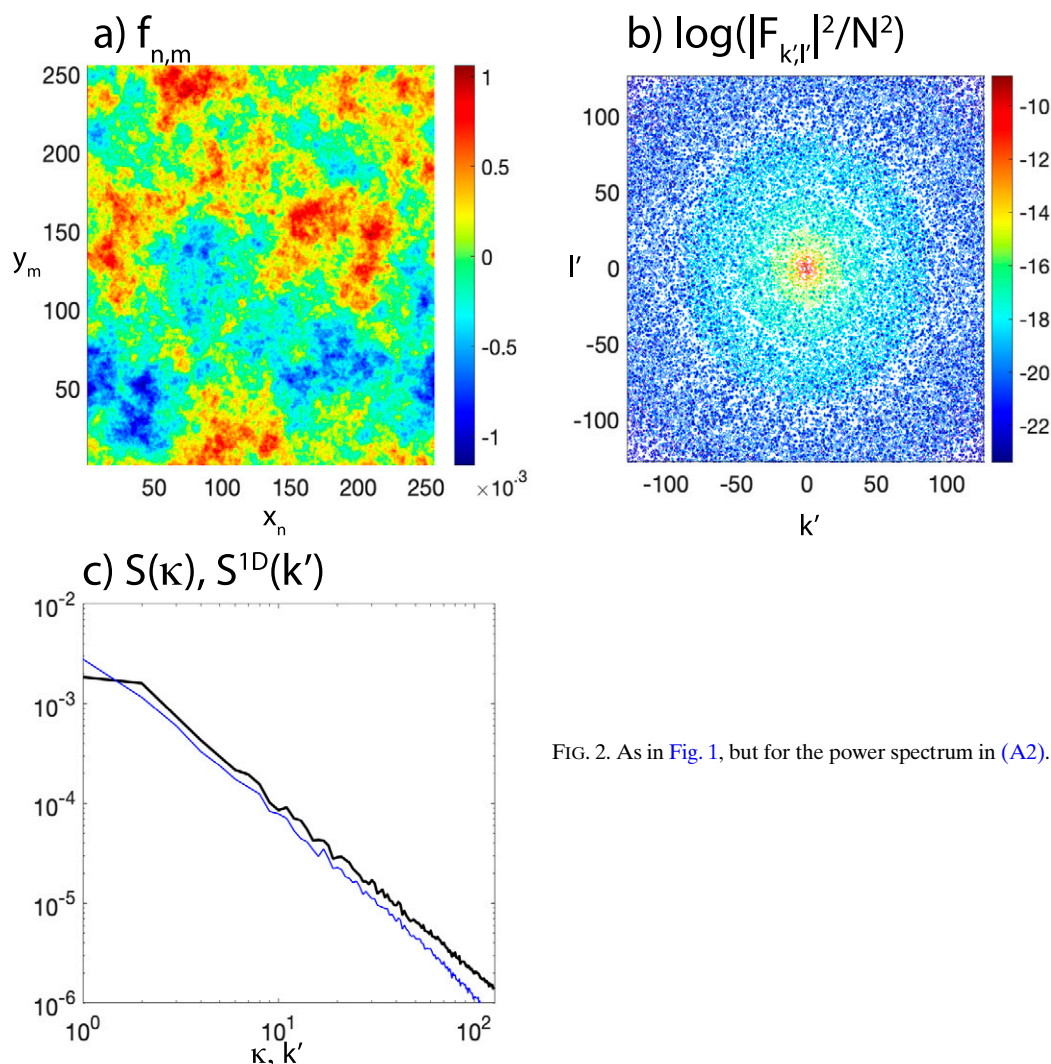


FIG. 2. As in Fig. 1, but for the power spectrum in (A2).

origin. Thus, the 2D power spectrum in (3) reduced to 1D is defined by

$$S(\kappa) = \frac{1}{N^2} \sum |F_{k',l'}|^2, \quad \kappa \leq \sqrt{k'^2 + l'^2} < \kappa + 1 \quad (9)$$

for  $0 \leq \kappa \leq N/2 - 1$ .

Equations (3) and (7) indicate  $N_y E^{1D} = E$  and that therefore the  $y_m$ -averaged-1D power spectrum compatible with (9) is

$$S^{1D}(k) = \sum_{m=1}^{N_y} |F_{k,m}^{1D}|^2 N_x^{-1}, \quad (10)$$

for  $1 \leq k \leq N$ . Substituting  $k'$  for  $k$  and letting  $N_x = N_y = N$  gives

$$S^{1D}(k') = \alpha_{k'} \sum_{m=1}^N |F_{k',m}^{1D}|^2 N^{-1}, \quad (11)$$

for  $-N/2 \leq k' \leq N/2 - 1$ . The factor  $\alpha_{k'} = 1$  for  $|k'| = 0$  or  $N/2$  and  $\alpha_{k'} = 2$  for  $0 < |k'| < N/2$ , which reflects the symmetry of  $|F_{k',m}^{1D}|^2$  about  $k' = 0$ .

### 3. Comparison of 1D $\kappa$ and 1D $k$

#### a. Simple examples

Consider the real, random function  $f_{n,m}$  on a square grid shown in Fig. 1a (see the appendix). Its power spectrum  $|F_{k',l'}|^2/N^2$  is shown in Fig. 1b. The power spectra  $S(\kappa)$  and  $S^{1D}(k')$  are shown in Fig. 1c. One observes that  $S^{1D}(k')$  is nearly independent of  $k'$  for  $k' < k'_{\text{peak}}$ . The reason for this is clear in light of (8). Substitution of (8) into (10) gives

$$S^{1D}(k) = \sum_{l=1}^{N_y} |F_{k,l}|^2 (N_x N_y)^{-1}, \quad (12)$$

or in terms of  $(k', l')$  and for  $N_x = N_y = N$ ,

$$S^{1D}(k') = \alpha_{k'} \sum_{l'=-N/2}^{N/2-1} |F_{k',l'}|^2 (N)^{-2}, \quad (13)$$

for  $0 \leq |k'| \leq N/2$ . The flat-line shape of  $S^{1D}(k')$  for  $k' < k'_{\text{peak}}$  is a result of the summation over  $l'$  of the nearly circularly symmetric  $|F_{k',l'}|^2/N^2$ .

In a second example, consider the random function  $f_{n,m}$  shown in Fig. 2a with the logarithm of the power spectrum shown in Fig. 2b. In this case the power spectrum follows a power law (“−5/3” in this example). In the appendix, the power spectral density for a power law can be obtained from (A2) as  $\tilde{F}\tilde{F}^* = A^2\kappa^{(\alpha-1)}$  with  $S(\kappa) = 2\pi\kappa\tilde{F}\tilde{F}^* = 2\pi A^2\kappa^\alpha$ . In continuous form the rhs of (8) implies  $S^{1D}(k) = (1/2a)\int_{-a}^a \tilde{F}\tilde{F}^* dl = (1/2a)\int_{-a}^a A^2(k^2 + l^2)^{(\alpha-1)/2} dl$ ; letting  $\chi = ll/k$ , the integral reduces to  $k^\alpha(A^2/2a)\int_{-\chi_1}^{\chi_1} (1 + \chi^2)^{(\alpha-1)/2} d\chi$  where the latter integral is just a numerical factor. Thus, for a power law, both  $S(\kappa)$  and  $S^{1D}(k)$  have the same power-law dependence. In terms of the discussion in the previous paragraph, in the power-law case  $k'_{\text{peak}} = 0$ .

b. Discussion

- 1) All calculations of error spectra based on statistical predictability theory treat fields such as that as shown in Fig. 1a with spectral densities that are exactly circularly symmetric (due to ensemble averaging, which is not done in our examples). Hence any comparison of meteorological-model error spectra with statistical predictability theory must be done with 2D spectral densities reduced to 1D spectra, as described in Errico (1985) and done here with the definition of  $S(\kappa)$  in (9).
- 2) Reducing a nearly circularly symmetric 2D spectrum to 1D using the  $y$ -averaged Fourier transforms in  $x$  [here defined as  $S^{1D}(k')$ ] leads to spectra like that in Fig. 1c in which the shape of the spectrum is independent of  $k'$  for  $k' < k'_{\text{peak}}$ . A power-law spectrum is the exception since  $k'_{\text{peak}} = 0$  (Fig. 2c).
- 3) Consider the following hypothetical case of upscale error growth from statistical predictability theory: Using (15) with  $\phi = 0$  generates a circularly symmetric 2D spectrum; letting the error amplitude  $A(t)$  increase as  $k'_{\text{peak}}(t)$  decreases with time produces the  $S(\kappa, t)$  and  $S^{1D}(k', t)$  shown in Fig. 3. The same data analyzed through  $S^{1D}(k', t)$  give the impression that the growth in time of the error spectra is “up-amplitude” rather than upscale since  $S_{1D}(k')$  is constant across scales for  $k' < k'_{\text{peak}}(t)$ .

4. Relevance of statistical predictability theory to atmospheric predictability

Using a high-resolution global model, Judt (2018) performed “identical-twin” type experiments in a case study of a specific 3-week period. The study showed that, initially, error growth was tied to moist convection and therefore highly localized, followed by a phase during which the error grew in scale, magnitude, and spatial extent. At approximately 2–3 weeks into

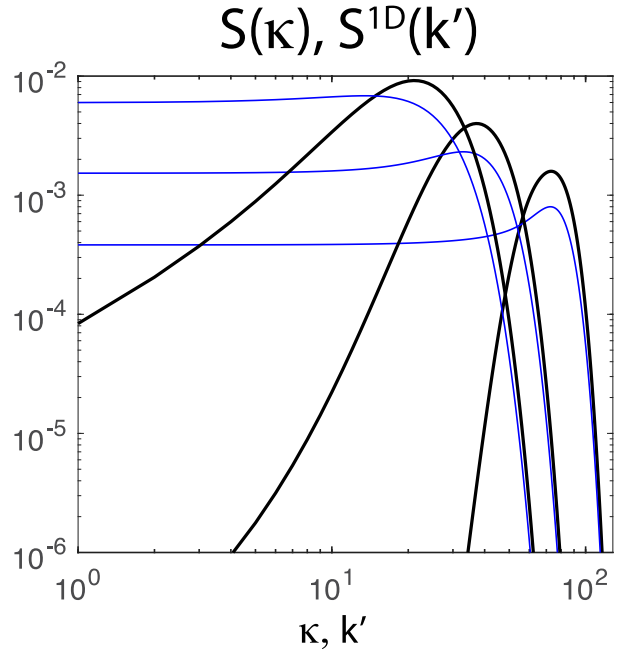


FIG. 3. As in Fig. 1c, but for three Gaussian spectra generated with (15) using  $\phi = 0$  and  $k_w = 20$  with  $(A, \kappa_c) = (0.5, 80)$ ,  $(1.0, 40)$ , and  $(2.0, 80)$ .

the forecasts, the divergence of forecasts that had started from small differences in the initial conditions had led to errors as large as any sample drawn from a climatological distribution (i.e., predictability was lost).

Analysis of the growing error spectra (his Fig. 13) using spherical harmonics showed a good qualitative correspondence to statistical predictability theory. More specifically, at the earliest times, the error growth rate was maximum at the smallest resolved scales, producing spectra that peaked at those scales and fell off toward low wavenumbers (Fig. 4a). After a few hours, the peak of the error spectra began shifting toward larger scales (i.e., up-scale growth; see crosses in Fig. 4a) while the rate of growth decreased. Overall, this behavior is expected for a “−5/3” background spectrum. The characteristics of error growth changed qualitatively after the peak of the error spectra had propagated through the mesoscales. Between day 5 and 10, the error spectra grew at a constant rate while peaking at the scale of the energy-containing eddies (~4000 km wavelength), as is expected for a “−3” background spectrum (Fig. 4b).

In an attempt to isolate error spectra over finite bands of latitude, Judt (2020) subjected the error fields to zonal Fourier transforms averaged over latitude. The resulting error spectra (his Fig. 5) are quite unlike the error spectra obtained via spherical harmonics and exhibit the “flat-line” shape for low wavenumbers. One of the motivations for the present paper was to understand how such different spectral shapes could be produced by the same physical-space error field. Motivated by the simple examples comparing  $S(\kappa)$  and  $S^{1D}(k')$ , we produced the spectral analysis in Fig. 4, with Figs. 4a and 4b the

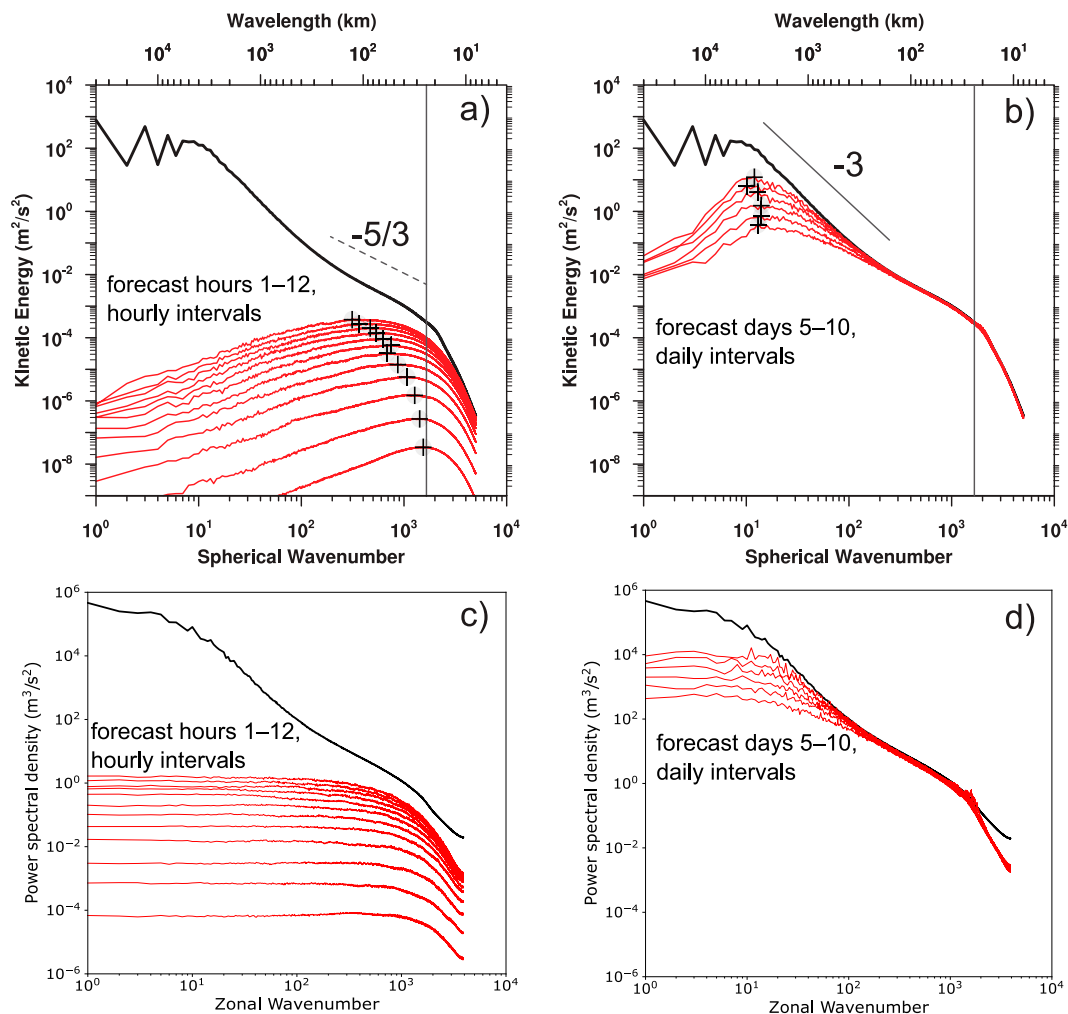


FIG. 4. Spectral error growth in the predictability experiment of Judt (2018). The evolution of the 250 hPa error kinetic energy spectra (a) between 1 and 12 h and (b) between 5 and 10 days as computed via spherical harmonics [same as Figs. 13a,b in Judt (2018)]. (c),(d) The corresponding spectra computed via Fourier transforms in longitude and averaged over latitude (60°S–60°N). The background spectra (black) are multiplied by 2. Crosses in (a) and (b) mark the peaks of the error spectra.

same as Figs. 13a and 13b of Judt (2018). The new analysis in Figs. 4c and 4d shows the latitudinal average of the zonal Fourier transforms from 60°S to 60°N. In both the “ $-5/3$ ” and the “ $-3$ ” cases, the error spectra in Figs. 4c and 4d show flat-line behavior over the low wavenumbers, similar to the simple examples. The close qualitative correspondence of the different reductions of 2D to 1D error spectra between the global model and the simple examples above is, we believe, good prima facie evidence that the 2D global-model error spectra have at least a qualitative similarity to the circularly symmetric 2D error spectra of statistical predictability theory.

### Discussion

1) The growth of the error spectra for 2D turbulence (Lesieur 2008, chapter 11) could be described as “up-amplitude,” except that it is peaked at the energy-containing scales of the

mean flow. We note that this behavior is based on a model of isotropic homogeneous 2D turbulence; in contrast, explanations of “up-amplitude” growth of error in the literature (e.g., Durran et al. 2013, p. 1482) are based on the inhomogeneous nature of turbulence in meteorological models.

- 2) The time evolution of the error spectra in Figs. 4a and 4b starts from the early stage upscale growth characteristic of a “ $-5/3$ ” background spectra (Fig. 4a) to the later stage of self-similar growth with peak at the scale of the energy-containing eddies characteristic of a “ $-3$ ” background spectra (Fig. 4b). As shown in Figs. 4c and 4d analysis using 1Dk-type error spectra produces a flat-line low-wavenumber spectrum in either case, thus significantly reducing the distinction between the two regimes.
- 3) A qualitative difference relative to statistical predictability theory is that upscale error evolution begins before the error spectrum is saturated at any scale, whereas in theory,

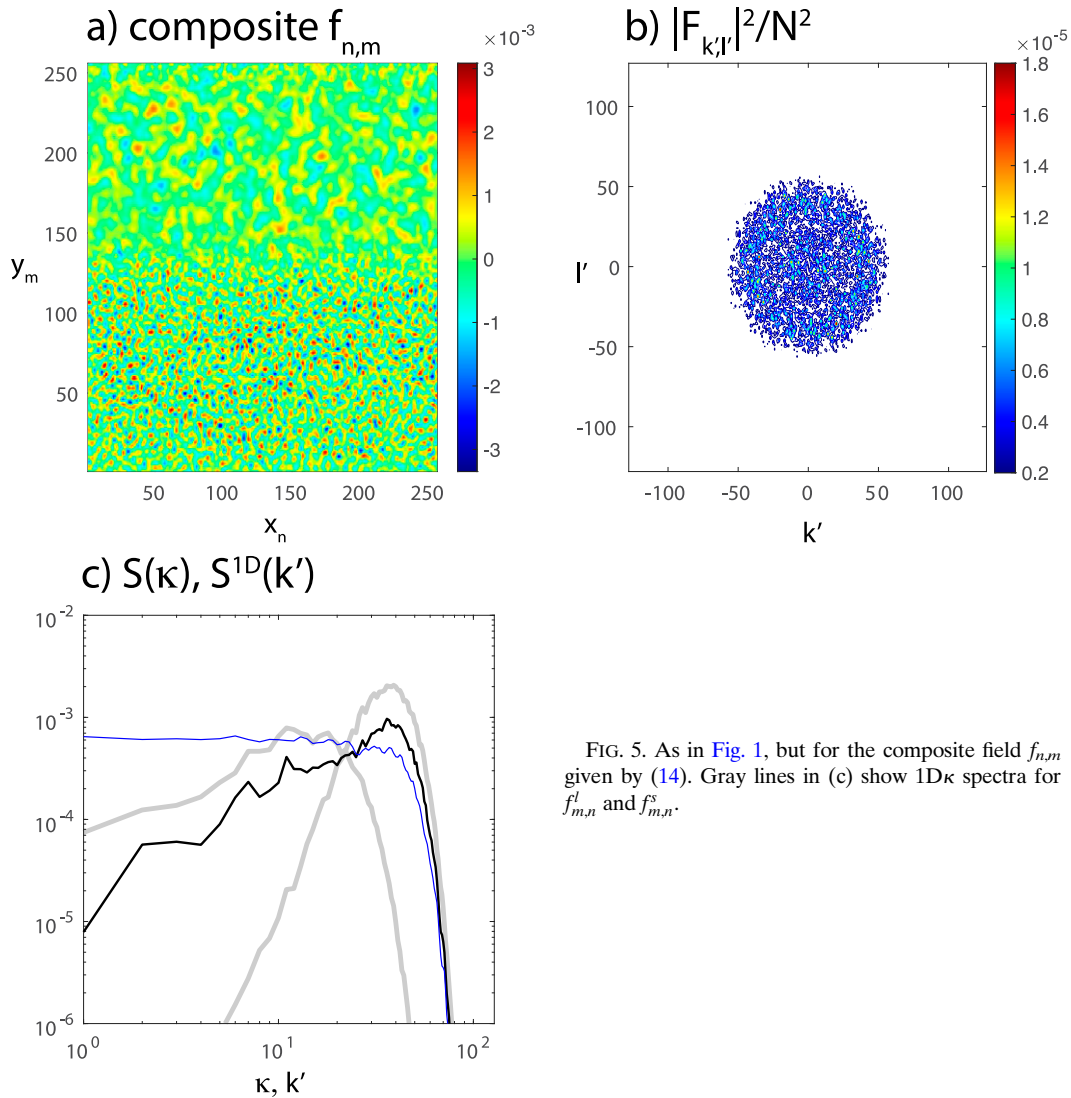


FIG. 5. As in Fig. 1, but for the composite field  $f_{n,m}$  given by (14). Gray lines in (c) show 1D  $k$  spectra for  $f_{m,n}^l$  and  $f_{m,n}^s$ .

the upscale evolution begins only once the spectrum is saturated at some scales. We hypothesize that this is a manifestation of the inhomogeneity of real atmospheric flows. The fastest error growth is extremely localized in space—confined to regions of deep convection in simulations of  $O(1)$  km resolution like that shown in Fig. 4, as first emphasized by Zhang et al. (2003). Nonlinear effects, including the slowing of error growth and upscale error evolution, will then also be spatially localized and can occur before any scale in the error spectrum is saturated.

### 5. “Local” spectra for inhomogeneous fields

Real atmospheric flows are not globally homogeneous and isotropic, which leads directly to considering predictability in specific subdomains of the globe, such as latitude bands or regions. One might hope that the tools of statistical predictability theory, which rest on assumptions of homogeneity and isotropy,

could still be applied on subdomains where those assumptions are more closely met.

This raises the question of how to evaluate the scale and other spectral characteristics of perturbations on a given subdomain. Indeed, it at least partly motivates the use of 1D  $k$  spectra, for example by separating the tropics, midlatitudes and polar regions as in Judt (2020). If 1D  $k$  spectra are not particularly well suited to predictability studies, as we argue here, then how should we perform spectral analysis of perturbations for limited subdomains of the globe?

Before proposing an answer, we consider first an inhomogeneous generalization of the example from section 3a and Fig. 1. Let  $f_{m,n}^s$  and  $f_{m,n}^l$  be “small-scale” and “large-scale” fields, whose Fourier transforms are given by (A1) with  $(A, \kappa_c) = (1, 40)$  or  $(1, 10)$ , respectively. The field we will consider is a composite, with statistics like  $f_{n,m}^s$  and thus small scale in the southern part of the domain, and like  $f_{n,m}^l$  and

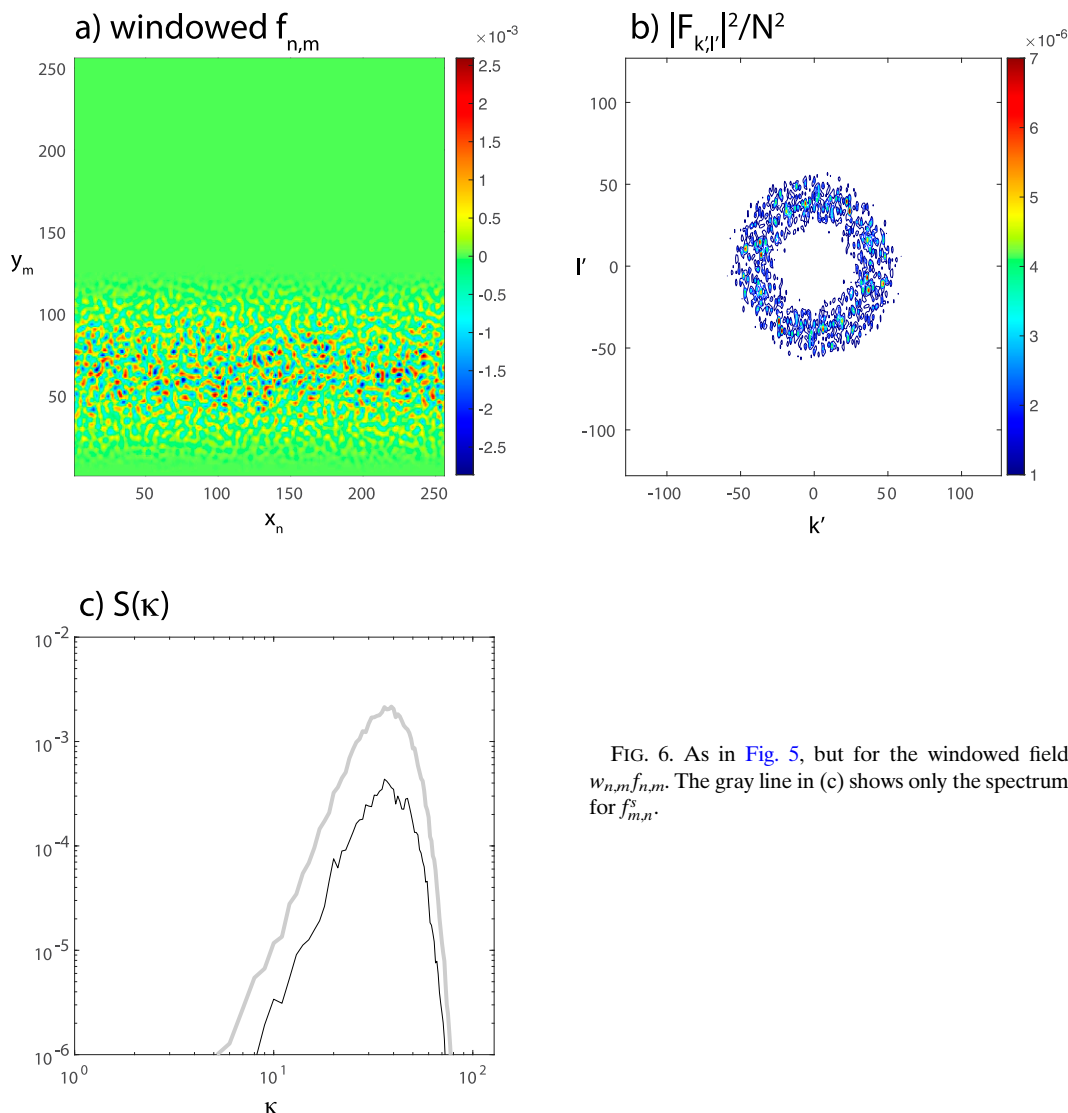


FIG. 6. As in Fig. 5, but for the windowed field  $w_{n,m}f_{n,m}$ . The gray line in (c) shows only the spectrum for  $f_{m,n}^s$ .

thus larger scale in the northern part of the domain. The field  $f_{n,m}$  has the following explicit form:

$$f_{n,m} = \alpha_m f_{n,m}^s + (1 - \alpha_m) f_{n,m}^l. \quad (14)$$

The weighting function  $\alpha_m$  is given by

$$\alpha_m = \frac{1}{2} \left( \frac{1 + \sqrt{1 + \epsilon \sin y_m}}{\sqrt{\sin^2 y_m + \epsilon}} \right),$$

and is approximately 1 in the southern half of the domain ( $y_m \approx \pi/2$ ) and zero in the north ( $y_m \approx 3\pi/2$ ), with a transition whose width is controlled by  $\epsilon$ . We take  $\epsilon = 0.2$ , which gives  $f_{n,m}$  shown in Fig. 5a.

The 2D and 1D  $\kappa$  spectra for the composite field appear in Figs. 5b and 5c, respectively. With different scales in the two halves of the domain, the 1D  $\kappa$  spectrum lacks the annular structure seen in Fig. 1b. The 1D  $\kappa$  spectrum (solid line) is a

melding of the spectra from  $f_{n,m}^l$  and  $f_{n,m}^s$  (which are shown as thick gray lines in Fig. 5c): at large wavelengths the spectrum follows that of  $f_{n,m}^l$ , and at small wavelengths that of  $f_{n,m}^s$ . As expected, the 1D  $\kappa$  spectrum shown in Fig. 5c is flat at large scales, unlike the 1D  $\kappa$  spectra for any of  $f_{m,n}$ ,  $f_{n,m}^l$ , or  $f_{n,m}^s$ .

We seek an analysis technique that will correctly identify local spectra and dominant scales of the composite field. The simplest approach is to multiply the original global field by a spatially localized window function that is confined to the local region of interest, and then compute the 1D  $\kappa$  spectrum of the resulting windowed, global field. Wong and Skamarock (2016) apply this technique to remove boundary effects when computing spectra for limited-area models, and similar approaches can be found in other fields of geophysics (Wieczorek and Simons 2005).

Figure 6 illustrates this approach applied to the composite  $f_{m,n}$ . The windowed field  $w_{n,m}f_{m,n}$  is shown in Fig. 6a for the window function:

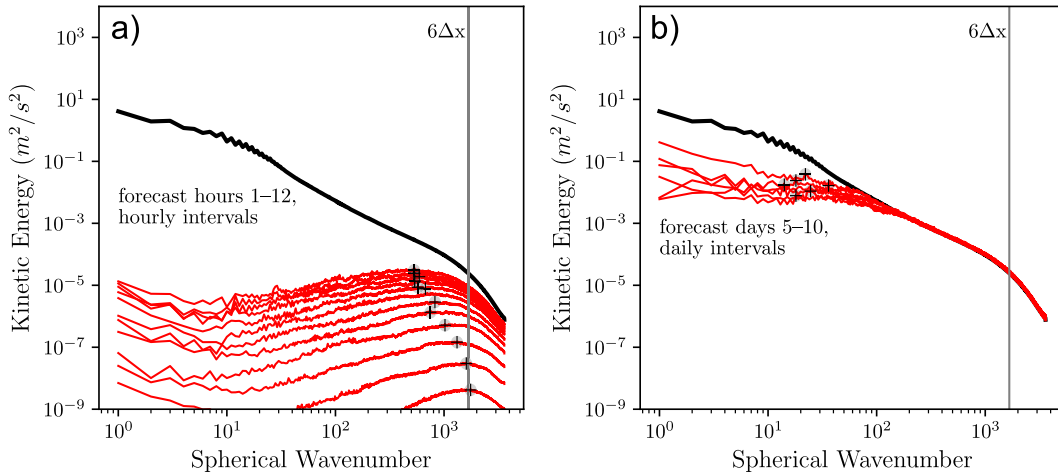


FIG. 7. As in Figs. 4a and 4b, but for the windowed field where the error field is multiplied by a Hann window function with bounds from 10°S to 10°N. Because of the artifacts at the largest scales (see text), only spectral peaks at wavenumbers > 10 are considered for marking with crosses.

$$w_{m,n} = \begin{cases} \sin^2 y_n & \text{if } y_n < \pi, \\ 0 & \text{if } y_n \geq \pi. \end{cases}$$

This function, usually written in terms of a cosine with twice the frequency, is known as the Hann window (Press et al. 2007, section 13.4), but we have explored other choices and any reasonable window with a spatial scale that is broad compared to the scale of  $f_{m,n}^s$  gives qualitatively similar results (not shown). Taking the 2D FFT of  $w_{m,n}f_{m,n}$  and then forming the 1D $\kappa$  spectrum yields the results in Figs. 6b and 6c. The 1D $\kappa$  spectrum of the windowed field accurately reproduces that of the small-scale field  $f_{m,n}^s$  that dominates the behavior of the global field in the southern half of the domain, except for an overall shift in amplitude. For fields whose variance is locally spatially homogeneous, that shift can be removed by normalizing the spectrum of the windowed field by  $N^2/\sum_{m,n}w_{m,n}^2$ , thus accounting for the point-wise reduction of amplitude of the windowed field.

For a “real-world” example of windowing, we applied the Hann window with bounds from 10°S to 10°N to the high-resolution simulation of Judd (2018) (Fig. 7). As expected from the examples in section 3, this method yields a slope for the background spectrum that is very close to that seen in 1D $\kappa$  spectra computed over 10°S–10°N [Fig. 5a in Judd (2020)]. This windowing method also captures the upscale evolution of the error in the tropics, with a decrease of the peak wavenumber for the 1D $\kappa$  spectra similar to that seen in the global 1D $\kappa$  error spectra in Fig. 4. In contrast, the 1D $k$  spectra for the errors [also displayed in Fig. 5a of Judd (2020)] show little indication of upscale evolution, again consistent with the examples in section 3.

The 1D $\kappa$  error spectra in Fig. 7, which are based on horizontal velocities on the sphere, exhibit an artifact at the largest scales that does not appear in the idealized, planar example of Fig. 6. Specifically, the error spectra bend upward for scales comparable to or larger than the scale of the window (roughly wavenumber 10 in this case). The cause of this artifact is not

obvious to us, but it does not limit the ability of the windowed 1D $\kappa$  spectra to capture the upscale error evolution.

### 6. Conclusions

Measures of error growth in meteorological forecast models are primary tools for assessing atmospheric predictability. The spatial patterns of an error field are often analyzed through Fourier decomposition to determine the prominent error-growth length scales. It has become common<sup>2</sup> to take the latitudinal average of the Fourier transform in the zonal direction to reduce 2D error spectra to 1D (1D $k$  spectra). These 1D $k$  error spectra are roughly independent of scale from large to small scales (basically a “flat line”) and maintain this form as the error spectra grow with time. Such growth of the error spectra is said to be “up-amplitude.” In contrast, statistical predictability theory predicts error spectra that are circularly symmetric in 2D wavenumber space with peak amplitude at a finite scale. These theoretical 2D spectra are reduced to 1D through integration around annuli in wavenumber space as a function of wavenumber magnitude  $\kappa$  (1D $\kappa$  spectra). These error spectra increase from nearly zero at large scales toward a peak at smaller scales and maintain this form as the error spectra grow with time. Since the smaller-scale peak wavenumber decreases with time (in the “–5/3” case), such growth of the error spectra is said to be upscale. The purpose of this note is to show that the two methods (1D $k$  and 1D $\kappa$ ) of reducing 2D spectra to 1D are not the same, except in the special case of a power-law spectrum.

We show that 1D $\kappa$  spectrum from a hypothetical error field typical of statistical predictability theory exhibits the

<sup>2</sup> In addition to the references in section 1, there are Zhang et al. (2019, their Figs. 6–8), Snyder et al. (2003, their Fig. 5), and McWilliams and Chow (1981, their Fig. 28). Figure 4 shows that 1D $k$  is still useful for estimating predictability limits as the same saturation time comes from both the 1D $\kappa$  and 1D $k$  analyses.

“flat-line” low-wavenumber signature seen in many such analyses in the literature. A hypothetical case of an error spectra growing in amplitude with a decreasing peak scale, illustrates the “up-amplitude” versus upscale descriptions. The relevance of statistical predictability theory was shown in Fig. 13 of Judt (2018) and partly reproduced here as Figs. 4a and 4b. Using the same dataset, Figs. 4c and 4d show that 1D $k$ -type error spectra exhibit the low-wavenumber flat-line shapes while their 1D $\kappa$ -type counterparts in Figs. 4a and 4b do not.

Finally, we suggest how 1D $\kappa$  spectra can be computed on spatial subdomains, which is a useful diagnostic tool for error fields that have spatially inhomogeneous statistics.

Although the analyst is at liberty to choose either 1D $k$  or 1D $\kappa$  error spectra, only the latter forms a basis for comparison of meteorological-model error spectra and the predictions of statistical predictability theory. If one chooses the former, then a dynamical interpretation must be based on an error equation resulting from a consistent application of a Fourier decomposition and averaging of the governing equations. We are unaware of any such equation in the literature.

*Data availability statement.* The output from the global high-resolution simulations in Figs. 4 and 7 can be made available upon request.

## APPENDIX

### Hypothetical Error Fields and Spectra

To create the function  $f_{n,m}$  shown in Fig. 1a, we first define

$$\tilde{F}_{k,l} = A \exp \left[ - \frac{(\sqrt{k^2 + l^2} - \kappa_c)^2}{\kappa_w^2} + 2\pi i \phi(k,l) \right], \quad (\text{A1})$$

where  $\phi(k, l)$  is a random number ranging from 0 to 1,  $\kappa_c$  is the wavenumber-space radius of the annulus of maximum  $|\tilde{F}|$  and  $\kappa_w$  is the width of its Gaussian distribution. The real part of the inverse Fourier transform of (A1) gives the  $f_{n,m}$  in Fig. 1a; the Fourier transform of  $f_{n,m}$  is used to construct the power spectrum is shown in Fig. 1b which is subsequently used for the 1D $\kappa$  and 1D $k$  spectra shown in Figs. 1c and 1d. The parameters used for Fig. 1 are  $A = 1$ ,  $\kappa_c = 40$  and  $\kappa_w = 20$ .

For the power-law case shown in Fig. 2, we define

$$\tilde{F}_{k,l} = A(\sqrt{k^2 + l^2})^{(\alpha-1)/2} \exp[2\pi i \phi(k,l)] \quad (\text{A2})$$

(with  $\alpha = -5/3$  and  $A = 10$ ) and follow the steps outlined in the previous paragraph.

Figure 3 is constructed using (A1) but with  $\phi = 0$  and then following the steps outlined above. Cases are shown with  $(A, \kappa_c) = (0.5, 80), (1.0, 40), (2.0, 20)$  to emulate error spectra with decreasing peak wavenumber  $\kappa_c$  and increasing amplitude.

## REFERENCES

Durran, D. R., P. A. Reinecke, and J. D. Doyle, 2013: Large-scale errors and mesoscale predictability in Pacific Northwest

- snowstorms. *J. Atmos. Sci.*, **70**, 1470–1487, <https://doi.org/10.1175/JAS-D-12-0202.1>.
- , J. A. Weyn, and M. Q. Menchaca, 2017: Practical considerations for computing dimensional spectra from gridded data. *Mon. Wea. Rev.*, **145**, 3901–3910, <https://doi.org/10.1175/MWR-D-17-0056.1>.
- Errico, R. M., 1985: Spectra computed from a limited area grid. *Mon. Wea. Rev.*, **113**, 1554–1562, [https://doi.org/10.1175/1520-0493\(1985\)113<1554:SCFALA>2.0.CO;2](https://doi.org/10.1175/1520-0493(1985)113<1554:SCFALA>2.0.CO;2).
- Judt, F., 2018: Insights into atmospheric predictability through global convection-permitting model simulations. *J. Atmos. Sci.*, **75**, 1477–1497, <https://doi.org/10.1175/JAS-D-17-0343.1>.
- , 2020: Atmospheric predictability of the tropics, middle latitudes, and polar regions explored through global storm-resolving simulations. *J. Atmos. Sci.*, **77**, 257–276, <https://doi.org/10.1175/JAS-D-19-0116.1>.
- Lesieur, M., 2008: *Turbulence in Fluids*. 4th ed. Springer, 558 pp.
- Lloveras, D. J., L. H. Tierney, and D. R. Durran, 2021: Mesoscale predictability in moist midlatitude cyclones is not sensitive to the slope of the background kinetic energy spectrum. *J. Atmos. Sci.*, **79**, 119–139, <https://doi.org/10.1175/JAS-D-21-0147.1>.
- Lorenz, E. N., 1969: The predictability of a flow which possesses many scales of motion. *Tellus*, **21**, 289–307, <https://doi.org/10.3402/tellusa.v21i3.10086>.
- Mapes, B. E., S. Tulich, T. Nasuno, and M. Satoh, 2008: Predictability aspects of global aqua-planet simulations with explicit convection. *J. Meteor. Soc. Japan*, **86A**, 175–185, <https://doi.org/10.2151/jmsj.86A.175>.
- McWilliams, M. C., and J. H. S. Chow, 1981: Equilibrium geostrophic turbulence I: A reference solution in a V-plane channel. *J. Phys. Oceanogr.*, **11**, 921–949, [https://doi.org/10.1175/1520-0485\(1981\)011<0921:EGTIAR>2.0.CO;2](https://doi.org/10.1175/1520-0485(1981)011<0921:EGTIAR>2.0.CO;2).
- Press, W. H., S. A. Teukolsky, W. T. Vetterling, and B. P. Flannery, 2007: *Numerical Recipes in C: The Art of Scientific Computing*. 3rd ed. Cambridge University Press, 1256 pp.
- Rotunno, R., and C. Snyder, 2008: A generalization of Lorenz’s model for the predictability of flows with many scales of motion. *J. Atmos. Sci.*, **65**, 1063–1076, <https://doi.org/10.1175/2007JAS2449.1>.
- Snyder, C., T. M. Hamill, and S. B. Trier, 2003: Linear evolution of error covariances in a quasigeostrophic model. *Mon. Wea. Rev.*, **131**, 189–205, [https://doi.org/10.1175/1520-0493\(2003\)131<0189:LEOECI>2.0.CO;2](https://doi.org/10.1175/1520-0493(2003)131<0189:LEOECI>2.0.CO;2).
- Weyn, W. A., and D. R. Durran, 2017: The dependence of the predictability of mesoscale convective systems on the horizontal scale and amplitude of initial errors in idealized simulations. *J. Atmos. Sci.*, **74**, 2191–2210, <https://doi.org/10.1175/JAS-D-17-0006.1>.
- Wieczorek, M. A., and F. J. Simons, 2005: Localized spectral analysis on the sphere. *Geophys. J. Int.*, **162**, 655–675, <https://doi.org/10.1111/j.1365-246X.2005.02687.x>.
- Wong, M., and W. C. Skamarock, 2016: Spectral characteristics of convective-scale precipitation observations and forecasts. *Mon. Wea. Rev.*, **144**, 4183–4196, <https://doi.org/10.1175/MWR-D-16-0183.1>.
- Zhang, F., C. Snyder, and R. Rotunno, 2003: Effects of moist convection on mesoscale predictability. *J. Atmos. Sci.*, **60**, 1173–1185, [https://doi.org/10.1175/1520-0469\(2003\)060<1173:EOMCOM>2.0.CO;2](https://doi.org/10.1175/1520-0469(2003)060<1173:EOMCOM>2.0.CO;2).
- , Y. Q. Sun, L. Magnusson, R. Buizza, S.-J. Lin, J.-H. Chen, and K. Emanuel, 2019: What is the predictability limit of midlatitude weather? *J. Atmos. Sci.*, **76**, 1077–1091, <https://doi.org/10.1175/JAS-D-18-0269.1>.